Drag force in the open-loop control of the cylinder wake in the laminar regime

B. Protas[a)]
Department of Aerodynamics, Institute of Aeronautics and Applied Mechanics, Warsaw University of Technology, ul. Nowowiejska 24, 00-665 Warsaw, Poland
and Laboratoire de Physique et Mécanique des Milieux Hétérogènes, UMR 7636 CNRS, École Supérieure de Physique et de Chimie Industrielles, 10 rue Vauquelin, 75231 Paris Cedex 05, France

J. E. Wesfreid
Laboratoire de Physique et Mécanique des Milieux Hétérogènes, UMR 7636 CNRS, École Supérieure de Physique et de Chimie Industrielles, 10 rue Vauquelin, 75231 Paris Cedex 05, France

(Received 26 October 2000; accepted 13 November 2001)

In this paper we are interested in identifying the physical mechanisms that accompany mean drag modifications in the cylinder wake flow subject to rotary control. We consider simple control laws where the obstacle rotates harmonically with frequencies varying from half to more than five natural frequencies. In our investigation we analyze the results of the numerical simulations at Re=150. All the simulations were performed using the vortex method, which in the paper is outlined and benchmarked. We confirm the earlier findings concerning mean drag reduction at higher forcing frequencies and show that for the considered values of Re this control technique is energetically inefficient. The main result is that changes of the mean drag are achieved by modifying the Reynolds stresses and the related mean flow correction. The controlled flows are carefully characterized in terms of these fields. Drag reduction is related to elongation of the recirculation bubble. It is argued that mean drag reduction is associated with control driving the mean flow toward the unstable symmetric state (the basic flow). © *2002 American Institute of Physics.* [DOI: 10.1063/1.1432695]

I. INTRODUCTION

Bluff body wakes play a very important role in various engineering applications. This is mainly due to the presence of big concentrated eddies, the so-called Bénard–von Kármán vortices, which are intrinsically related to forces acting on the obstacle. Furthermore, bluff body wakes possess several intriguing features, e.g., strong mean flow effects (see Zielińska *et al.*[1,2]), which also make their study very interesting from the physical point of view. The effective control of wake flows constitutes a challenge in fluid dynamics. From the implementation point of view, one of the simplest control methods is the rotary motion of the obstacle. This configuration is shown in Fig. 1. One of the first attempts at the rotary control of the cylinder wake was made by Taneda.[3] Then this technique was systematically studied in the laboratory by Tokumaru and Dimotakis,[4] who by applying a very simple sinusoidal control law at Re=15 000 obtained a remarkable modification of the flow pattern, including significant suppression of vortex shedding, accompanied by substantial drag reduction. This effect was further investigated under various flow and control conditions by other researchers, e.g., Filler *et al.*[5] studied the response of the separated shear layers to small amplitude oscillations, Lu and Sato[6] focused on the modifications of the flow patterns due to control, Shiels[7] and Shiels and Leonard[8] primarily studied the Reynolds number effect on vortex dynamics in the controlled flows, Beak and Sung[9,10] and Fujisawa *et al.*[11,12] investigated the wake behavior in the presence of lock-on, whereas Baek *et al.*[13] studied the secondary and tertiary lock-on. In a recent study Cheng *et al.*[14] presented a comprehensive analysis of the flow pattern modifications occurring at and close to lock-on in the controlled flows. In another recent investigation, He *et al.*[15] used the tools of the optimal control theory to optimize the frequency and amplitude of harmonic oscillations. Our objective in the present study is to revisit this control strategy in the laminar regime and with a fairly broad range of forcing frequencies, in a similar vein as was done by Tokumaru and Dimotakis.[4] We will use the theory of slightly supercritical wakes to unravel the critical physical mechanisms accompanying the observed drag reduction with a particular focus on modifications of the mean velocity and the Reynolds stress fields. An analysis of these mechanisms and how they are affected by the rotary control constitutes the primary objective of this paper. We presume that the crucial mechanisms remain similar in the controlled wake flows at higher values of the Reynolds number. Another issue we will also address here is the power budget of the controlled flows. This work is a computational study. We simulate here the plane infinite wake flow at the Reynolds number Re=150. The structure of the paper is as follows: in Sec. II we present

[a)]Author to whom correspondence should be addressed. Present address: Department of Mechanical and Aerospace Engineering, University of California—San Diego, 9500 Gilman Drive, La Jolla, California 92093-0411; telephone: (858) 822 3391; fax: (858) 822 3107; electronic mail: bprotas@ucsd.edu

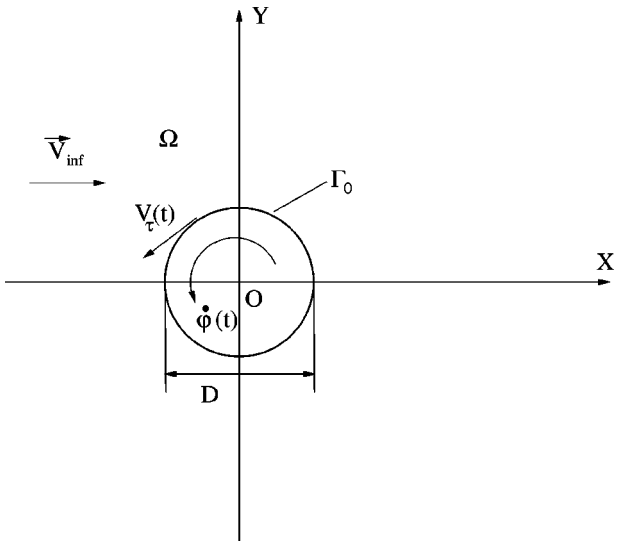

FIG. 1. Flow configuration with control.

some both rigorous and phenomenological concepts related to slightly supercritical wake flows, with a particular emphasis on the relation between the mean fields and the hydrodynamic forces; then we briefly introduce the vortex method used in all the simulations and validate it by presenting some standard benchmarks; this is followed by a presentation of the results of the numerical simulations; a discussion of these results from the perspective developed in this work concludes the paper. In Appendix A we present qualitative analysis of the Poisson equation linking pressure modifications and the Reynolds stresses. In Appendix B we give some more details concerning the fundamentals and implementation of the vortex method.

II. WAKE FLOWS: PHENOMENOLOGY AND BEYOND

The standard phenomenological model (see, e.g., Mathis *et al.*[16] and Dušek *et al.*[17]) for the wake dynamics near the Hopf bifurcation predicts that, when the Reynolds number reaches its critical value Re_c, the steady symmetric state becomes unstable and bifurcates to a periodic solution. In the supercritical regime the steady symmetric state still exists, but is unstable and as such cannot be obtained in laboratory conditions. As will be shown later, it can nevertheless be easily obtained in numerical simulations. This solution is often referred to as the *basic state* (e.g., Zielińska *et al.*[1] and Ref. 2). It was proposed by Dušek *et al.*[17] and Dušek[18] that every hydrodynamic quantity in the saturated supercritical wake flow (i.e., for $t\to\infty$) be represented as a sum of a certain steady field, i.e., the basic flow, and a superposition of harmonics. This proposition presupposes that the velocity field in the whole flow domain oscillates with the same single global frequency, a property known as the *global mode* behavior (e.g., Goujon-Durand *et al.* in Ref. 19; Zielińska and Wesfreid in Ref. 1). Here we give this representation in terms of the streamfunction Ψ_∞,

$$\Psi_\infty(x,y,t)=\Psi_b(x,y)+\sum_{n=-\infty}^{\infty} c_n(x,y)e^{in\gamma t}, \tag{1}$$

where Ψ_b is the streamfunction corresponding to the basic flow, and c_n are the spatial envelopes associated with the particular harmonics. All relevant flow quantities can be recovered by applying suitable differential operators to Ψ_∞, and this procedure naturally carries over to the spatial envelopes of the harmonics. The amplitude of oscillations with frequency $n\gamma$ (i.e., the nth harmonic) at the point (x_0,y_0) is given by $2|c_n(x_0,y_0)|$. This quantity thus represents the spatial variation of the oscillation amplitude and therefore has often been referred to as the *global mode* amplitude (e.g., Zielińska *et al.*[1] and Dušek[18]). All oscillations vanish at infinity, hence we have the property $\lim_{(x,y)\to 0}|c_n|\to 0$. The symbol γ denotes the fundamental frequency of vortex shedding at saturation. This frequency is often normalized to give the Strouhal number of the natural vortex shedding $\mathrm{St}_{\mathrm{nat}}=\gamma D/|\mathbf{V}_\infty|$. As a matter of fact, relation (1) is the limiting case (for $t\to\infty$) of a more general relation, allowing for a slow evolution of the envelopes c_n, the so-called ''slow dynamics.'' Here we consider the saturated case when all transients have died out, hence the time dependence of the envelopes c_n is suppressed. The basic flow Ψ_b is the unstable solution of the steady-state Navier–Stokes system obtained for a supercritical value of Re. Structurally, it is related to the solution obtained in the subcritical conditions and is characterized by symmetry with respect to the centerline. When a representation of the form (1) is now plugged into a bilinear expression (like the nonlinear term in the Navier–Stokes equation), then one of the terms we obtain is proportional to $\Sigma_{n,m=-\infty}^{\infty} c_n c_m e^{i(n+m)\gamma t}$. It is straightforward to observe that when $m=-n$, i.e., when the nth harmonic interacts with its complex conjugate, this results in a zero frequency (stationary) mode. In other words, the presence of a fluctuating field gives rise to a steady correction to the background field. This phenomenon is a particular example of the triadic interaction (for modes with frequencies 0, $n\gamma$, and $-n\gamma$). This zero frequency mode is conventionally named the *nonlinear mean flow correction*. Its characteristics in various hydrodynamic instabilities are surveyed by Craik in Ref. 20, whereas the properties of this field in the wake flow were recently investigated by Zielińska *et al.*[2] It was shown that this field accounts for the remarkable alteration of the mean velocity profile and shortening of the recirculation length observed in unsteady wakes. On the other hand, it is well known that the time series of drag consists of even harmonics, whereas lift consists of odd harmonics. This motivates looking at the zero mode, i.e., the first even harmonic in Eq. (1), as regards sources of the mean drag modifications.

Taking the time average (denoted $\langle\cdot\rangle$) of Eq. (1), we obtain $\langle\Psi_\infty(x,y,t)\rangle=\Psi_b(x,y)+c_0(x,y)$. Thus, every mean quantity in the supercritical regime consists of two parts: the basic field and the mean flow correction (the zeroth mode). In agreement with this, the mean drag c_D also consists of the two contributions: (i) the drag c_D^b of the basic flow that at a given Re is fixed and cannot be modified, and (ii) the drag c_D^0 of the mean flow correction that represents the average influence of the oscillatory flow and can be modified by suitable manipulation of the Bénard–von Kármán vortices,

$$c_D=c_D^b+c_D^0. \tag{2}$$

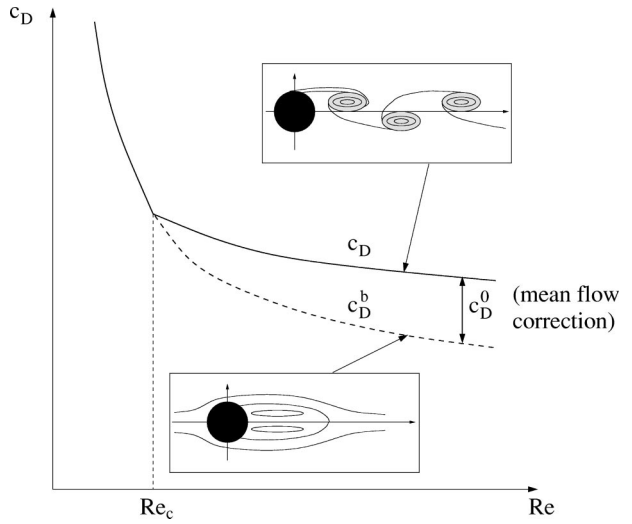

FIG. 2. Schematic showing the increase of drag due to the appearance of vortex shedding and the related mean flow correction. The insets represent the structure of the basic flow (drag indicated by the dashed line) and the unsteady flow (drag indicated by the solid line) at a given supercritical Re.

As will be discussed in detail below, the mean flow correction arises due to nonlinear self-interaction of the oscillatory part of the flow. Its drag c_D^0 increases the total drag of the flow, which is schematically shown in Fig. 2. Obviously, the mean drag can be entirely characterized using the mean fields (including the Reynolds stresses). Thus, our main interest in this paper is to analyze the relation between the oscillatory flow components, the nonlinear mean flow correction, and the drag. Below we derive the equation governing the behavior of the nonlinear mean flow correction, and see how this field contributes to drag. At every point the velocity may be split into its mean $\mathbf{V}^m$ and fluctuating part $\mathbf{V}'$ as $\mathbf{V}=\mathbf{V}^m+\mathbf{V}'$, where $\langle\mathbf{V}\rangle=\mathbf{V}^m$ and $\langle\mathbf{V}'\rangle=0$. In accordance with the remarks made above, the mean field can be further split, thus

$$\mathbf{V}^m=\mathbf{V}^b+\mathbf{V}^0, \tag{3}$$

where $\mathbf{V}^b$ represents the basic flow, i.e., the unstable, steady, and symmetric state, and $\mathbf{V}^0$ is the mean flow correction (the zeroth mode). It should be remarked here that decomposition (3) is fairly general and does not involve any assumptions. The same decomposition can be made for pressure. We restrict our attention here to the case when the *mean* value of the boundary velocity, i.e., the control, is zero. This is naturally satisfied by any time-periodic forcing. Now we take the time-averaged Navier–Stokes equation in the conservative form ($\mathbf{a}\otimes\mathbf{b}$ denotes the dyadic product of the two vectors $\mathbf{a}$ and $\mathbf{b}$, i.e., $[\mathbf{a}\otimes\mathbf{b}]_{ij}=a_ib_j$),

$$\begin{aligned}
&\nabla\cdot(\mathbf{V}^m\otimes\mathbf{V}^m)=-\nabla p^m+\mu\Delta\mathbf{V}^m-\nabla\cdot\langle\mathbf{V}'\otimes\mathbf{V}'\rangle,\\
&\nabla\cdot\mathbf{V}^m=0,\\
&\mathbf{V}^m=0,\quad \text{on the boundary } \Gamma_0,\\
&\mathbf{V}^m\to\mathbf{V}_\infty,\quad \text{for } |x|\to\infty,
\end{aligned} \tag{4}$$

the equation for the basic flow (i.e., the steady state Navier–Stokes equation),

$$\begin{aligned}
&\nabla\cdot(\mathbf{V}^b\otimes\mathbf{V}^b)=-\nabla p^b+\mu\Delta\mathbf{V}^b,\\
&\nabla\cdot\mathbf{V}^b=0,\\
&\mathbf{V}^b=0,\quad \text{on the boundary } \Gamma_0,\\
&\mathbf{V}^b\to\mathbf{V}_\infty,\quad \text{for } |x|\to\infty,
\end{aligned} \tag{5}$$

and subtract the latter from the former. Using decomposition (3), we obtain

$$\begin{aligned}
&\nabla\cdot(\mathbf{V}^0\otimes\mathbf{V}^0)=-\nabla p^0+\mu\Delta\mathbf{V}^0-\nabla\cdot(\mathbf{V}^0\otimes\mathbf{V}^b+\mathbf{V}^b\otimes\mathbf{V}^0)\\
&\qquad\qquad -\nabla\cdot\langle\mathbf{V}'\otimes\mathbf{V}'\rangle,\\
&\nabla\cdot\mathbf{V}^0=0,\\
&\mathbf{V}^0=0,\quad \text{on the boundary } \Gamma_0,\\
&\mathbf{V}^0\to0,\quad \text{for } |x|\to\infty.
\end{aligned} \tag{6}$$

This is the equation that governs the behavior of the mean flow correction $\mathbf{V}_0$ (i.e., the zeroth mode) arising due to the nonlinear self-interaction of the oscillatory part of the flow. The last two terms on the rhs have the form of the divergence of the dyadic tensors: the first of them represents interaction of the mean flow correction $\mathbf{V}^0$ with the basic flow $\mathbf{V}^b$ and the second the influence of the fluctuating part of the flow. The second term thus involves the Reynolds stress tensor $\langle\mathbf{V}'\otimes\mathbf{V}'\rangle$. As a matter of fact, when oscillatory control is applied, the term $\nabla\cdot\langle\mathbf{V}'\otimes\mathbf{V}'\rangle$ indirectly represents its effects on the mean flow correction, and therefore also on the associated mean drag c_D^0. The relation between the mean flow correction and the Reynolds stresses was first studied by Maurel *et al.* in Ref. 21.

It is well known (see, e.g., Henderson in Ref. 22) that in bluff body wakes the main contribution to drag comes from pressure. At Re=150 pressure drag constitutes approximately 81% of the total drag. Thus, drag modifications are mainly achieved by changing the pressure drag and below we focus on how the pressure drag is affected by the oscillatory part of the flow. In this we follow the ideas developed by Mittal and Balachandar in Ref. 23. Taking the divergence of the first equation in the system (6), we obtain

$$\begin{aligned}
&\Delta p^0=\overbrace{-\nabla\cdot[\nabla\cdot(\mathbf{V}^0\otimes\mathbf{V}^0)+\nabla\cdot(\mathbf{V}^0\otimes\mathbf{V}^b+\mathbf{V}^b\otimes\mathbf{V}^0)]}^{\Delta p^{0b}}\\
&\qquad\underbrace{-\nabla\cdot[\nabla\cdot\langle\mathbf{V}'\otimes\mathbf{V}'\rangle]}_{\Delta p^{0rs}},\\
&(\mathbf{n}\cdot\nabla)p^0=\underbrace{\mu\Delta V_n^0|_\Gamma}_{(\mathbf{n}\cdot\nabla)p^{0bc}}.
\end{aligned} \tag{7}$$

We see that, due to linearity of the Poisson equation, the solution of (7) can be represented as the sum $p^0=p^{0bc}+p^{0b}+p^{0rs}$. In Eq. (7) we schematically indicate the rhs and boundary terms associated with each element in this sum. The first term (p^{0bc}) is related to the Neumann-type boundary conditions in (7). The term p^{0b} corresponds to the influence of the mean flow correction field $\mathbf{V}^0$ and its interaction with the basic flow $\mathbf{V}^b$ [i.e., the first divergence term on the rhs in (7)]. The term p^{0rs} represents the effect of the Rey-

nolds stresses [i.e., the last term on the rhs in (7)]. Owing to the nature of the relation (7), we will say that the fields p^{0b} and p^{0bc} represent the *indirect* influence, and the field p^{0rs} the *direct* influence, of the Reynolds stresses on the pressure drag. It was shown by Mittal and Balachandar in Ref. 23 that in the case of the bluff body wake the field p^{0b} is essentially insensitive to modifications of the Reynolds stresses. Conversely, the field p^{0rs} was shown to strongly depend on their distribution. Based on this observation we will assume that the effect of the Reynolds stresses on the pressure drag is mainly contained in the field p^{0rs} that satisfies the following equation:

$$\Delta p^{0rs} = -\nabla\cdot[\nabla\cdot\langle \mathbf{V}'\otimes\mathbf{V}'\rangle],$$
$$(\mathbf{n}\cdot\nabla)p^{0rs} = 0. \tag{8}$$

The above assumption is particularly true when the compared flows have similar mean velocity fields. In Appendix A we analyze this equation to assess how the magnitude and the distribution of the Reynolds stresses $\langle \mathbf{V}'\otimes\mathbf{V}'\rangle$ affect the quantity $\oint_{\Gamma_0} p^{0rs} n_x d\sigma$, i.e., the corresponding pressure drag. In Sec. IV we will use those results to link the changes of the Reynolds stress distribution and magnitude to drag modifications in the controlled flows.

III. NUMERICAL SIMULATIONS

In this section we very briefly introduce and validate our numerical method. In all the studies reported here we use the vortex method, which is described in some detail in Appendix B. Here we only present the system of partial differential equations governing the problem and show some standard benchmark tests for our method. In the present study we use the vortex method to solve the two-dimensional (2-D) vorticity transport equation,

$$\frac{\partial\omega}{\partial t} + (\mathbf{V}\cdot\nabla)\omega = \mu\Delta\omega,$$
$$\omega = \frac{\partial v}{\partial x} - \frac{\partial u}{\partial y}, \quad \frac{\partial u}{\partial x} + \frac{\partial v}{\partial y} = 0,$$
$$\mathbf{V} = \mathbf{V}_b \quad \text{on the boundary } \Gamma_0, \tag{9}$$
$$\mathbf{V} \to \mathbf{V}_\infty, \quad \text{for } |x| \to \infty,$$
$$\mathbf{V}|_{t=0} = \mathbf{V}_0, \quad \text{in } \Omega,$$

where $\mathbf{V}=[u,v]$ is the velocity field, ω the (scalar) vorticity field, and μ is the coefficient of viscosity. The system is complemented with a suitable initial condition $\mathbf{V}_0$ and the boundary conditions $\mathbf{V}_b$ and $\mathbf{V}_\infty$ representing, respectively, the velocity of the boundary and the free-stream velocity at infinity. Note that in the above vorticity equation both the initial and boundary conditions are expressed in terms of velocity, rather than vorticity. In exterior multiconnected domains (e.g., the 2-D cylinder wake), the above system must be complemented by an integral constraint on the vorticity produced on the boundary (e.g., Gunzburger and Peterson[24]). It ensures that wake energy remains finite at all times and that the pressure recovered *a posteriori* from the velocity and vorticity fields will be single-valued (e.g., Nowakowski *et al.*[25]). This constraint has the following form (it must be written for each "hole" in the computational domain):

$$\mu\int_0^L \frac{\partial\omega}{\partial n} d\sigma = \int_0^L \left(\frac{\partial\mathbf{V}}{\partial t}\cdot\boldsymbol{\tau} + (\mathbf{V}\cdot\mathbf{n})\omega\right) d\sigma, \tag{10}$$

where $\boldsymbol{\tau}$ stands for the wall-tangential versor. This constraint is obtained by projecting the Navier–Stokes equation on the direction tangential to the boundary, integrating it along the perimeter and then requiring that the pressure jump be equal to zero. This condition implies that the total diffusive vorticity flux across the boundary (equal to the amount of circulation produced on the boundary) must be compensated by angular acceleration of the body and the wall–normal vorticity advection. Obviously, the latter vanishes for circular obstacles.

Here we present only the most important benchmarks of the method. For further validation and as well as more imple-

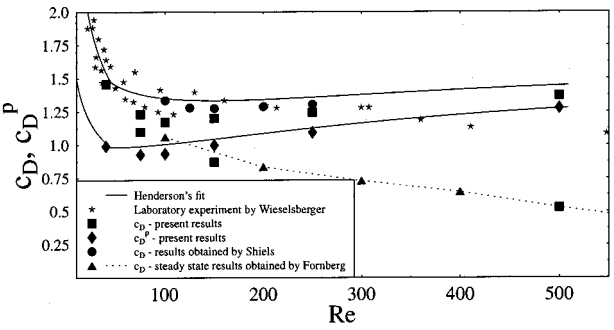

(a) The mean values of the total drag c_D and pressure drag c_D^p.

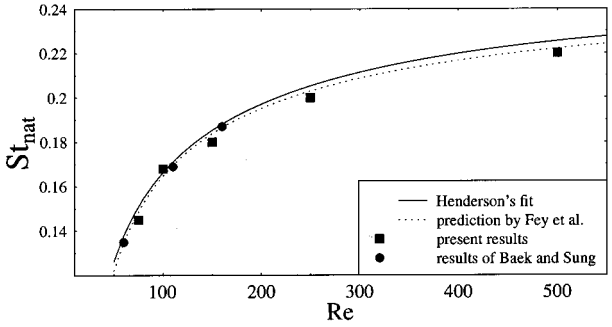

(b) Vortex shedding Strouhal number St_{nat}.

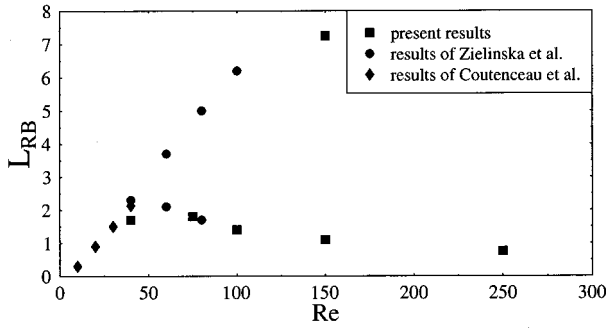

(c) Length of the recirculation bubble L_{RB}.

FIG. 3. A comparison of the dependence of the mean total and pressure drag (a), the vortex shedding Strouhal number (b), and the length of the recirculation bubble (c) on the Reynolds number for the present simulations and reference results available in the literature.

TABLE I. Numerical parameters used in the wake simulations with the rotary control at Re=150 and $W=2.0$. The maximum rotation angle is denoted $\varphi_{\max}$, the time step Δt, the blob radius r_b, and the approximate number of vortices N_b. The cases analyzed in greater detail are marked in boldface.

	St_f	$\frac{\mathrm{St}_f}{\mathrm{St}_{\mathrm{nat}}}$	$\varphi_{\max}$ (deg)	Δt	r_b	N_b ($\times 10^3$)
No control	⋯	⋯	⋯	**0.05**	**0.0178**	**300**
A	**0.09**	**0.5**	**406**	**0.05**	**0.0178**	**400**
B	0.16	0.89	228	0.05	0.0178	380
C	**0.18**	**1.0**	**203**	**0.05**	**0.0178**	**320**
D	0.20	1.11	183	0.05	0.0178	340
E	0.36	2.0	101	0.025	0.0178	270
F	0.70	3.89	52	0.0125	0.0178	240
G	**0.90**	**5.0**	**41**	**0.0125**	**0.0178**	**240**
H	1.00	5.56	37	0.0125	0.0178	240

mentation details the reader is referred to Protas.[26] In Fig. 3(a) we show the dependence of the mean total and pressure drag coefficients c_D and c_D^p on the Reynolds number. For Re=75, 150, and 500 we show two data points, the lower branch representing the unstable, steady symmetric solutions (the basic flows), and the upper the oscillatory flows. The two branches obviously correspond to the two curves schematically shown in Fig. 2. Our data is compared against the results obtained by Shiels[7] (also using a vortex method), Henderson's fit[22] approximating his results over a broad range of Re, the experimental dataset of Wieselberger,[27] and the steady-state results of Fornberg[28] (cf. the lower curve in Fig. 2). Note that, as explained by Mittal and Balachandar in Ref. 23, for Re higher than about 180, the 2-D computation tends to systematically overestimate drag. Next, in Fig. 3(b) we compare our results for the dependence of the Strouhal number of vortex shedding $\mathrm{St}_{\mathrm{nat}}$ on Re to the Henderson's fit summarizing his data,[29] the empirical relationship proposed by Fey *et al.* in Ref. 30 and the results obtained by Baek and Sung.[10] Finally, in Fig. 3(c) we show the dependence of the length of the recirculation bubble on the Reynolds number. Our results are compared against the experimental data of Coutanceau and Bouard[31] and the numerical data of Zielińska *et al.*[2] For supercritical values of Re (i.e., Re≥46) two branches are observed in Fig. 3(c): the lower one represents the mean values obtained in the oscillatory flows, whereas the upper corresponds to the unstable steady symmetric solutions (i.e., the basic flows). We conclude by saying that in all these benchmarks our results are in fair agreement with the available reference data.

IV. RESULTS OF THE SIMULATIONS

A. Control parameters

In the present section we proceed to discuss the controlled flows. In all the cases studied here control has the form of the rotary oscillation of the cylinder with the instantaneous rotation rate $\dot{\varphi}(t)$ given by the formula

$$\dot{\varphi}(t)=\dot{\varphi}_0 \sin(2\pi f t)=W\frac{2|\mathbf{V}_\infty|}{D}\sin\left(2\pi\,\mathrm{St}_f\frac{|\mathbf{V}_\infty|}{D}t\right), \quad (11)$$

where the frequency f and the rotation amplitude $\dot{\varphi}_0$ are expressed in terms of nondimensional parameters: the Strouhal number $\mathrm{St}_f=fD/|\mathbf{V}_\infty|$ and the normalized amplitude $W=\dot{\varphi}_0 D/(2|\mathbf{V}_\infty|)$ (which gives the ratio of the peak circumferential velocity to the free stream at infinity). These two parameters entirely characterize the control. In all our simulations we put $W=2.0$. According to the arguments presented by Tokumaru and Dimotakis in Ref. 4, this value is already sufficient for effective control. Our simulations are performed at Re=150, which is still before the onset of 3-D effects. In Table I we summarize the numerical parameters and also the parameters characterizing the forcing in all the runs. The forcing frequency St_f ranges from one-half to more than five natural shedding frequencies and for convenience the corresponding flows are labeled A–H. In the table we also indicate the maximum rotation angles (in degrees) in the various cases. For every forcing frequency our simulations are performed for some time after transients have died out and the saturated state has been reached, so that converged statistics can be obtained. Higher forcing frequencies required that a finer time step Δt should be used. Under such forcing conditions, however, the statistically steady state was reached much faster and the total computational time of the run remained comparable to that required at lower forcing frequencies.

The results of the simulations will be presented in the theoretical framework established in Sec. II. They will be shown for all the cases A–H detailed in Table I and will be compared against the uncontrolled flow at the same Reynolds number. Apart from this, we choose three sets of forcing conditions that we will analyze more closely: the subharmonic forcing (A), the resonant forcing (C), and the high-frequency forcing (G). These cases appear most representative for all the studied forcing conditions and are marked in boldface in Table I.

B. Flow patterns

We begin the discussion of the results with a brief analysis of the flow patterns in the controlled flows. In Fig. 4 we present the vorticity fields obtained in the numerical simulations. First, as a reference, in Fig. 4(a) we show the pattern obtained in the flow with no forcing. Then, Figs. 4(b)–4(i) correspond to the controlled flows with forcing as indicated (cases A–H). In all the figures solid lines represent positive,

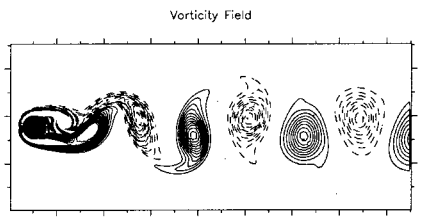

(a) no forcing

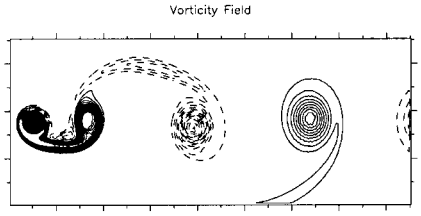

(b) $St_f = 0.09$ ($\frac{St_f}{St_{nat}} = 0.5$), $W = 2.0$

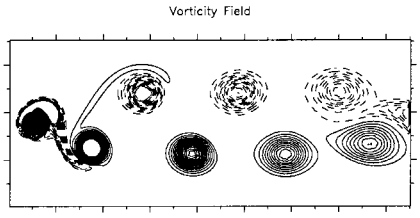

(c) $St_f = 0.16$ ($\frac{St_f}{St_{nat}} = 0.89$), $W = 2.0$

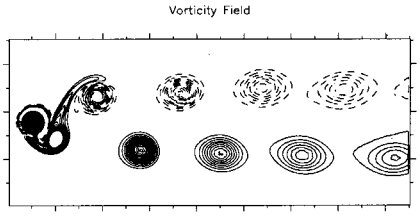

(d) $St_f = 0.18$ ($\frac{St_f}{St_{nat}} = 1.0$), $W = 2.0$

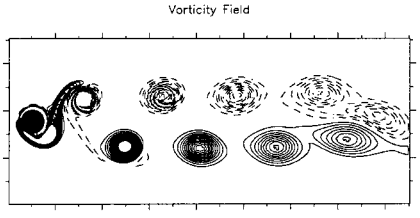

(e) $St_f = 0.20$ ($\frac{St_f}{St_{nat}} = 1.11$), $W = 2.0$

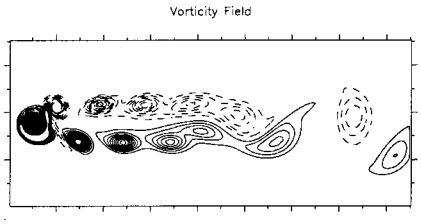

(f) $St_f = 0.36$ ($\frac{St_f}{St_{nat}} = 2.0$), $W = 2.0$

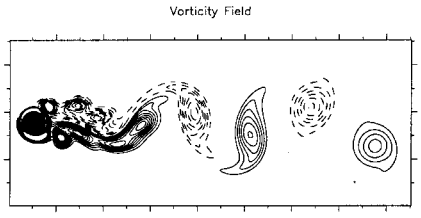

(g) $St_f = 0.70$ ($\frac{St_f}{St_{nat}} = 3.89$), $W = 2.0$

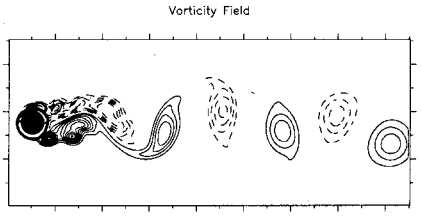

(h) $St_f = 0.90$ ($\frac{St_f}{St_{nat}} = 5.0$), $W = 2.0$

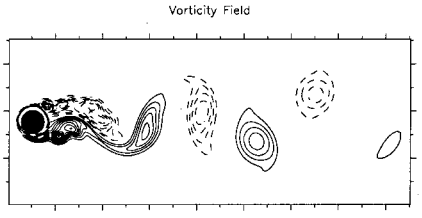

(i) $St_f = 1.00$ ($\frac{St_f}{St_{nat}} = 5.56$), $W = 2.0$

FIG. 4. The vorticity fields from the numerical simulations at Re=150 for the flows with no forcing and with the forcing conditions A through H. For clarity, the contour lines for the extremal vorticity values are not shown.

and dashed lines negative, vorticity values. In Fig. 4(a) one can see the familiar Bénard–von Kármán vortex street. In Fig. 4(b) (case A), it is replaced by big vortices with the wavelength twice as big as in the uncontrolled case. For the resonant and nearly resonant forcing conditions presented in Figs. 4(c)–4(e) (cases B, C, D) one can see the formation of two arrays of regular vortices that get rearranged downstream. Figure 4(f) (case E) represents an intermediate situation where regular vortices still exist, but are significantly less coherent. Finally, in Figs. 4(g)–4(i) (cases F, G, and H) corresponding to the highest forcing frequencies, we see that the Bénard–von Kármán vortices are noticeably weakened. The concentrated vorticity in the recirculation zone is disrupted and forms undulations with the wavelength corresponding to the forcing frequency. As a result, the vortex shedding is less intense comparing to the uncontrolled case. We note here that these observations are in agreement with the laboratory experiments reported by Goujon-Durand *et al.*[32] The simulations presented above produced huge volumes of data. Pointwise analysis of the velocity time series

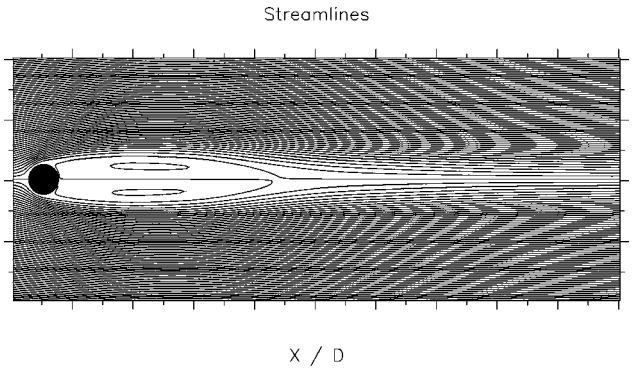

FIG. 5. Streamlines for the basic flow at Re=150.

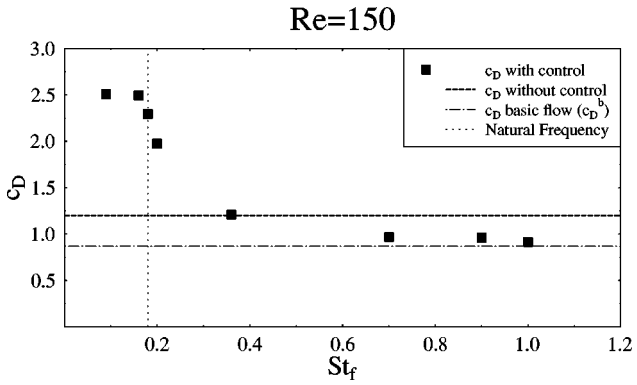

FIG. 6. The mean values of the drag coefficient c_D versus the forcing Strouhal number St_f for Re=150. The coefficients are also shown for the flow with no control and the basic flow.

(not shown here) allows us to classify the response of the system to forcing as follows: in cases B, C, D, where the forcing frequency is close to the natural frequency, the system oscillates with the forcing frequency and can be therefore considered ''locked,'' in cases A, E, and G the forcing frequency is a multiple of St_{nat} and harmonic frequencies are detected, whereas in cases F and H the forcing frequency is incommensurable with St_{nat} and the response of the system is quasiperiodic. Comparing to the quasiperiodic cases, the amplitude of the velocity fluctuations is increased in the locked states. As the forcing frequency crosses the natural frequency, the phase of vortex shedding exhibits a jump. All of these observations confirm that the present simulations are in agreement with standard reference results concerning forced wakes (e.g., Fujisawa *et al.*,[11] Lu and Sato,[6] Baek and Sung,[9] and Cheng *et al.*[14]).

We conclude our presentation of the flow patterns by showing the basic flow, i.e., the unstable steady symmetric solution of the Navier–Stokes system, also at Re=150. It was obtained in the numerical simulation using the technique described in Appendix B. This state obviously corresponds to no forcing. An infinitesimal perturbation can destabilize it and trigger the onset of vortex shedding. The basic state has significantly lower drag than the corresponding solution with vortex shedding [cf. the lower branches in Figs. 2 and 3(a)]. In Fig. 5 we show the streamline pattern of this flow, as streamlines apparently better than vorticity field characterize steady flows. A remarkable feature of this flow is the elongated recirculation bubble behind the cylinder [see also the unstable branch in Fig. 3(c)].

C. Drag

Inspection of Figs. 4(a)–4(i) shows that the rotary control significantly affects the shedding pattern and one can thus expect the drag force to vary under the different forcing conditions. To quantify this effect, in Fig. 6 we present the *mean* values of the drag coefficient c_D as a function of the forcing Strouhal number St_f. In this figure we also indicate the values of c_D characterizing the uncontrolled flow with the natural vortex shedding and the basic flow at the same Re. The vertical dotted line represents the Strouhal number of the natural vortex shedding (for Re=150, $St_{nat}=0.18$). The first observation to be made here is that the drag coefficient c_D is increased at lower and decreased at higher forcing frequencies. As regards the behavior of drag for nearly resonant forcing frequencies, our results are qualitatively consistent with those reported by Tokumaru and Dimotakis,[4] Lu and Sato,[6] Fujisawa *et al.*,[11] and by Cheng *et al.*[14] As the forcing frequency is decreased from the values slightly higher to slightly lower than the natural frequency, the drag coefficient sharply increases and reaches values approximately two times higher than in the uncontrolled case. This closely agrees with the results obtained by Cheng *et al.*[14] at Re =1000 and $W=2.0$. Results presented by those authors for different rotation amplitudes W, as well as the data reported by Fujisawa *et al.*[11] (Re=20 000, $W=0.1-0.38$) and by Tokumaru and Dimotakis[4] (Re=15 000, $W=2.0$) reveal the same qualitative trends. Different actual values of drag obtained in those studies show that the effect of control depends on the Reynolds number and the amplitude W of the rotary oscillations (higher Re results in lower drag for forcing close to resonant). In the cases G and H drag reduction reached about 25%, which is less than in the studies by Lu and Sato,[6] Shiels[7] and Tokumaru and Dimotakis.[4] However, all these investigations were performed at higher Re. This shows that the amount of drag reduction obtained by rotary control of the cylinder wake is Reynolds number dependent. As explained in Sec. II [cf. Fig. 2 and Eq. (2)], the mean drag in the cylinder wake comes from two contributions: the drag of the basic flow and the drag associated with the mean flow correction. Obviously, the variation of the mean drag observed in Fig. 6 was achieved by modifying the mean flow correction field. Further below we address this issue in greater detail. We also observe here that, as the forcing frequency increases, the values of the mean drag approach the value of drag in the basic flow (c_D^b), however, they never become smaller than that. Nonetheless, this does not imply that the mean drag coefficient monotonously decreases as the forcing frequency is increased. In fact, the simulations performed by the authors at Re=500 (not reported here), those by Cheng *et al.*[14] and by Lu and Sato[6] at Re=1000, He *et al.*[15] at Re=200 and Re=1000, and the laboratory experiments by Tokumaru and Dimotakis[4] at Re=15 000, suggest the presence of some optimal forcing frequency beyond which the mean drag increases. The value of this frequency again seems to depend on the Reynolds number and the ro-

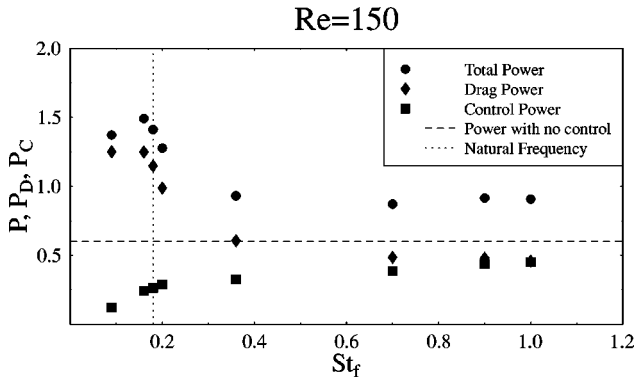

FIG. 7. The mean values of the drag power P_D, the control power P_C, and the total power P versus the forcing Strouhal number St_f for the controlled flows at Re=150. The power for the flow without control is also indicated.

tation amplitude. When the total drag in the controlled flow (c_D) approaches the drag in the basic flow (c_D^b), then this implies that the drag of the mean flow correction is driven to close to zero. This observation points to the following theoretical question: is it possible, under periodic forcing conditions, to obtain a flow with the mean drag lower than in the basic flow? In other words, is it possible to obtain a mean flow correction field with negative drag? For the case of the rotating cylinder this remains an open question. However, for the case of the pitching airfoil, a partially affirmative answer to this question was provided by the laboratory study by Lai and Platzer.[33]

D. Power budget

The modifications of drag discussed above were obtained at different costs in the various cases considered. Now, we proceed to analyze the energy budget of the controlled flows. In Fig. 7 we show the dependence of the mean drag power P_D, the control power P_C, and the total power $P=P_D+P_C$ on the forcing Strouhal number St_f. In the figure we also indicate the power in the flow with no forcing (the horizontal line) and the Strouhal number of the natural vortex shedding $\mathrm{St}_{\mathrm{nat}}$ (the vertical line). Computation of the control power is based on the torque M applied to the obstacle as $P_C=\langle M\dot{\varphi}\rangle$ and does not account for inertial effects related to the moment of inertia of the obstacle. In principle, the latter are entirely material dependent and as such can be arbitrary. The drag power is determined as the mean product of the drag force F_D and the free-stream velocity $P_D=\langle F_D|\mathbf{V}_\infty|\rangle$. In Fig. 7 we see that for higher forcing frequencies the drag power P_D decreases which is due to the drag reduction discussed above. This is, however, accompanied by a significant increase of the control power, so that the total power in all the cases far exceeds its value in the uncontrolled flow. The power saving ratio defined as

$$\mathrm{PSR}=\frac{\Delta P_D}{P_C} \tag{12}$$

is thus everywhere less than unity. On the other hand, the study by Shiels and Leonard[8] shows that for much higher values of the Reynolds number the PSR increases and at Re=15 000 reaches the level of $O(10)$. This implies that the energetic efficiency of this control technique depends on the Reynolds number and for small values of Re the control is energetically rather inefficient. The reason for this is that the flows at higher Re are more unstable and therefore less effort is required to push them toward a desired state, once a proper excitation mode has been determined.

E. Mean velocity fields

In Sec. II it was shown that the mean values of the drag and lift are intrinsically linked to the mean velocity fields and the Reynolds stresses. It was argued that the mean drag consists of the two contributions: the basic flow which at a given Re is fixed and cannot be modified, and the nonlinear mean flow correction field that results from self-interaction of the oscillatory part of the flow. Thus, by manipulating the way the Bénard–von Kármán vortices are created and advected, one can change the mean flow correction field and hence the drag. Below we will take a closer look at the mean velocity fields in the controlled flows, as they well represent the mean effect of control on the flow. In Fig. 8 we show the transverse profiles of the mean longitudinal velocity u_m at different downstream stations. The results are shown for the uncontrolled flows (top figure) and the flows with the forcing conditions A, C, and G. The mean fields are symmetric with respect to the centerline, so the data are shown for the upper part of the flow only. Complementary information is presented in Fig. 9, where we show the mean longitudinal velocity u_m on the centerline as a function of the downstream distance from the obstacle. First of all, we note that the uncontrolled flow and the flow with the forcing conditions G reveal a striking similarity as regards both longitudinal and transverse profiles. This implies that in the mean sense the wakes of these flows do not differ much. The only difference is that the controlled flow has a deeper and more elongated recirculation bubble. The subharmonic case (A) is characterized by a very quick recovery of the unperturbed flow velocity, with the recirculation bubble shrunk almost to zero. The profiles become bimodal downstream. On the other hand, the resonant forcing (case C) results in the profiles that change very little with the downstream distance. Consequently, such flow can be considered parallel in the mean sense and possessing a high degree of spatial organization. This property was already observed in Fig. 4(d). The above characteristics can be compared with the results reported by Tokumaru and Dimotakis (Fig. 3 in Ref. 4). For this purpose in Fig. 10 we combine the transverse profiles from Fig. 8 corresponding to the downstream station of $x/D=4.0$ (4.5 in Tokumaru and Dimotakis[4]). The profiles for both the natural shedding without forcing and the high-frequency forcing (case G) are characterized by Gaussian-like curves with comparable values. In the latter case the wake is somewhat deeper and narrower. In the study by Tokumaru and Dimotakis the wake deficit corresponding to the high-frequency forcing was remarkably smaller than in the unforced case. We relate this discrepancy to the Reynolds number effect (note that the drag reduction obtained in Ref. 4 at Re=15 000 was much bigger than in the present study at Re=150). Subharmonic forcing in both

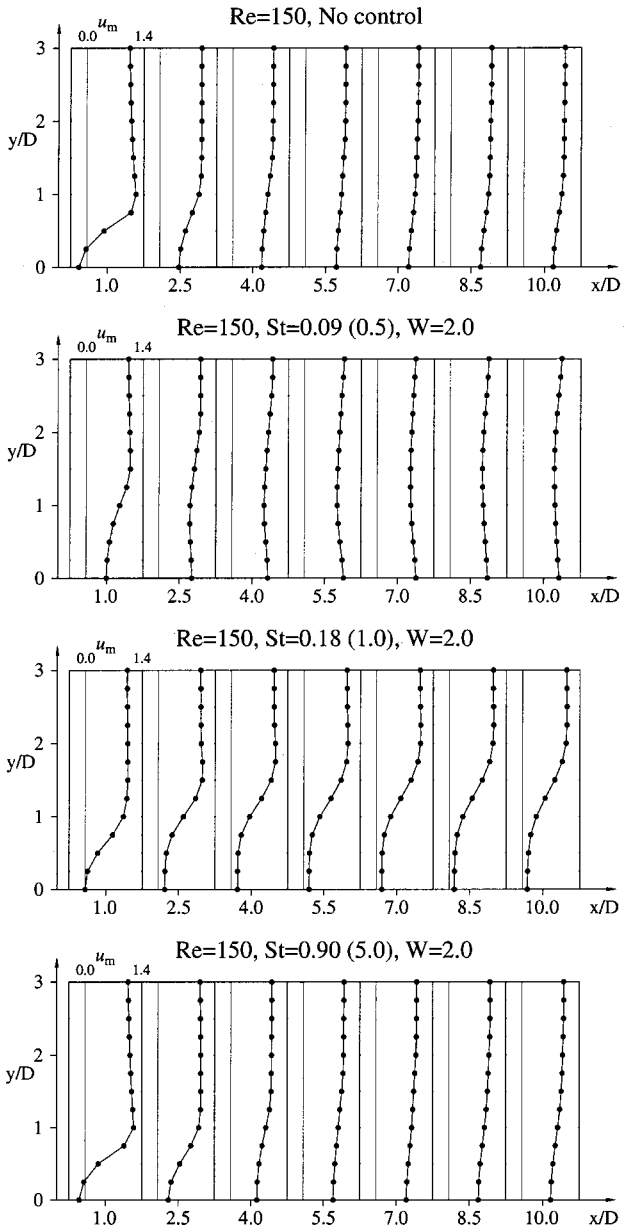

FIG. 8. The transverse profiles of the mean longitudinal velocity u_m at different downstream stations indicated on the abscissa for the flow without forcing and for the cases A, C, and G.

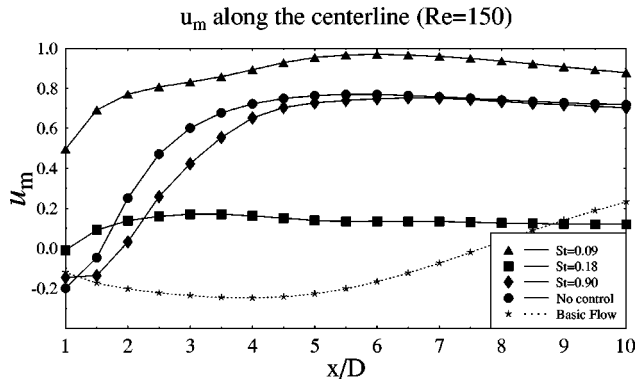

FIG. 9. Profiles of the mean longitudinal velocity u_m as a function of the downstream distance from the obstacle along the centerline for the cases A, C, and G, the flow without forcing and the basic flow.

studies resulted in the characteristic bimodal profile with minima located off the centerline. The profile corresponding to the resonant forcing (case C) is characterized by a deep and broad dip.

The feature that well characterizes the mean longitudinal velocity in the controlled flows is the length and shape of the recirculation bubble. In Fig. 11 we show the distributions of u_m in the near wake obtained in the simulations of the uncontrolled flow at Re=150 and the controlled flows A, C, and G. The boundary of the recirculation bubble (corresponding to $u_m=0$) is marked with a thick line. In this figure we see that in the case A representing the subharmonic forcing the recirculation bubble is effectively suppressed. In the case C (resonant forcing) it is considerably shrunken compared to the uncontrolled case. Conversely, in the case G (high-frequency forcing) the recirculation bubble is elongated. In all the cases except for A the shape of the bubble is preserved and characterized by a broadening close to the separation point on the cylinder boundary. In the case G the minimum of the longitudinal velocity is shifted toward the furthermost tip of the bubble. Information about the influence of the control on the length L_{RB} of the recirculation bubble is collected in Fig. 12, where we show the values of L_{RB} in the controlled flows normalized by its value in the uncontrolled flow as a function of the ratio $\mathrm{St}_f/\mathrm{St}_{\mathrm{nat}}$. In the figure we also indicate the length of the recirculation bubble in the basic flow at Re=150 (cf. Fig. 5). We see that for $\mathrm{St}_f/\mathrm{St}_{\mathrm{nat}}<3.5$ the recirculation bubble is shrunken compared to the uncontrolled flow. On the other hand, for $\mathrm{St}_f/\mathrm{St}_{\mathrm{nat}}>3.5$ the recirculation zone is elongated. These results can be summarized by saying that higher forcing frequencies result in longer recirculation bubbles and in this sense the obtained flows appear more similar to the basic flow.

As explained in Sec. II, the basic flow is fixed and modifications of the mean velocity profiles are achieved by changing the nonlinear mean flow correction through the Reynolds stresses. A distribution of the mean correction for the longitudinal velocity component $u_0=u_m-u_b$ shows how the mean flow is changed with respect to the unstable solution (the basic flow) due to the presence of vortex shedding and

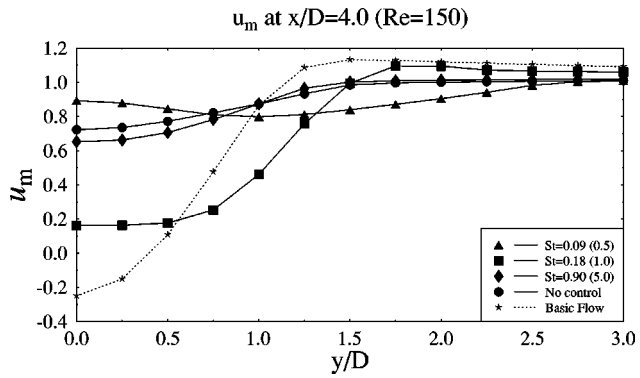

FIG. 10. The transverse profiles of the mean longitudinal velocity u_m at the downstream distance of $x/D=4.0$ for the flow without forcing, the basic flow and for the cases A, C, and G.

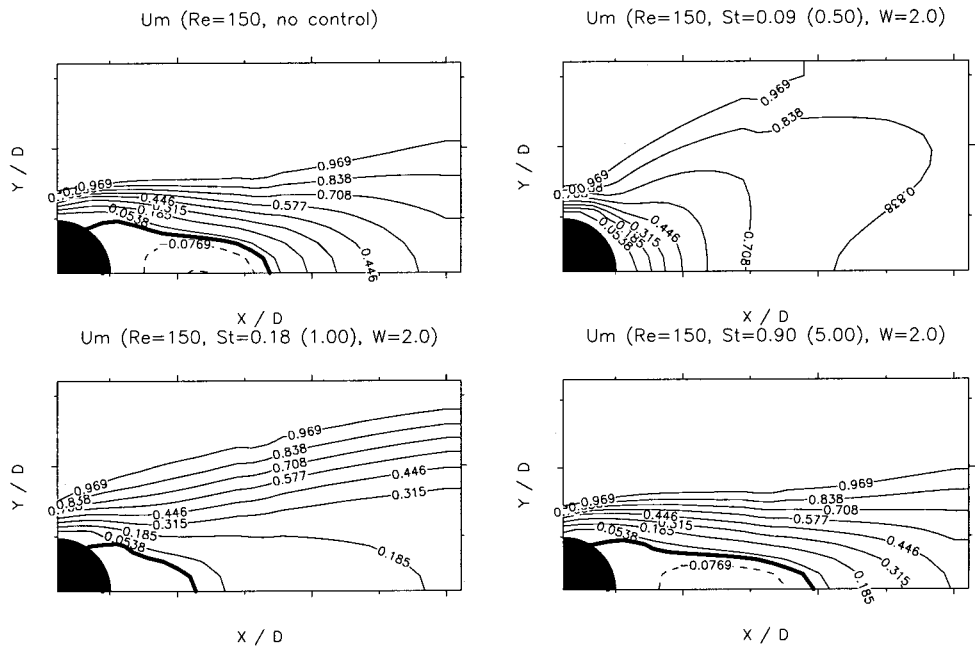

FIG. 11. The mean values of the longitudinal velocity u_m in the flow with no forcing and the flows with the forcing conditions A, C, and G. The thick lines correspond to $u_m=0$.

the related Reynolds stresses. This is also a convenient way to quantify the net effect of forcing on the mean flow. In Fig. 13 we show the distributions of the mean flow correction u_0 obtained in the simulations of the uncontrolled flow and the flows with the forcing conditions A, C, and G, at Re=150. In order to emphasize the areas where u_0 changes sign, the lines corresponding to $u_0=0$ are marked with thick lines. In areas where $u_0>0$ the vortex shedding accelerates the mean flow and decelerates elsewhere. In the case of the uncontrolled flow we see that the mean flow is slowed down in a small region just behind the obstacle and accelerated in a large rectangular area stretching downstream along the centerline. Away from the centerline the mean flow is slowed down. A similar distribution of the mean flow correction is obtained for the flow with the high-frequency forcing (case G), with the difference, however, that the values of u_0 in the region just behind the obstacle are generally smaller. The consequence of this is the elongated recirculation bubble already observed in Figs. 11 and 12. In the case C (resonant forcing) the region of negative u_0 behind the obstacle is shrunk and the area where the mean flow is accelerated gets narrower as one moves downstream. In the case of the subharmonic forcing (case A) there is no deceleration region behind the obstacle and the mean flow is accelerated everywhere along the centerline and decelerated away from it. In Fig. 13 we see that, except for the case G, the fields of the mean flow correction have significantly different distributions depending on the forcing frequency. In fact, as is evident from Eq. (6), these differences result from different distributions of the Reynolds stresses in the controlled flows. We proceed to discuss them below.

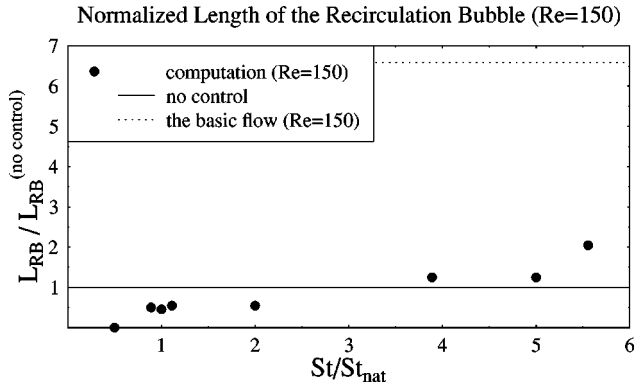

FIG. 12. Dependence of the length of the recirculation bubble in the controlled flows normalized by its value in the uncontrolled flow as a function of the ratio St_f/St_{nat}. The length of the recirculation bubble in the basic flow at Re=150 is also indicated.

F. Reynolds stresses

In Sec. II it was explained that, as regards drag in controlled flows, the importance of the Reynolds stresses is basically twofold, as they both directly and indirectly (i.e., through modifications of the mean flow) affect pressure drag [cf. Eq. (7)]. However, in situations when the *mean* flows are *similar* (e.g., the uncontrolled flow and the case G), it is evident from Eq. (7) that the major effect comes from the field p^{0rs} satisfying Eq. (8). To quantify this effect in Figs. 14(a)–14(c) we show the contour plots of the quantities $g_{uu}(x^0,y^0)=\oint_{\Gamma_0}(\partial^2/\partial x\partial x)\,G(x,y,x^0,y^0)|_{\Gamma_0}n_x d\sigma$, $g_{uv}(x^0,y^0)=2\oint_{\Gamma_0}(\partial^2/\partial x\partial y)\,G(x,y,x^0,y^0)|_{\Gamma_0}n_x d\sigma$ and $g_{vv}(x^0,y^0)=\oint_{\Gamma_0}(\partial^2/\partial y\partial y)\,G(x,y,x^0,y^0)|_{\Gamma_0}n_x d\sigma$ (see Appendix A for definitions and derivations), which show how the Reynolds stresses $\langle u'u'\rangle$, $\langle u'v'\rangle$, and $\langle v'v'\rangle$ acting at the point (x^0,y^0) add to the pressure drag. The actual contribution is obtained by multiplying the value of g_{uu}, g_{uv}, or g_{vv} at the given point by the corresponding Reynolds stress. Integrating over the whole domain and adding the three contributions yields the total pressure drag due to the Reynolds stresses (i.e., $\oint_{\Gamma_0}p^{0rs}n_x d\sigma$). The contour plots of g_{uu} and g_{vv} are symmetric, and of g_{uv} antisymmetric, with respect to the

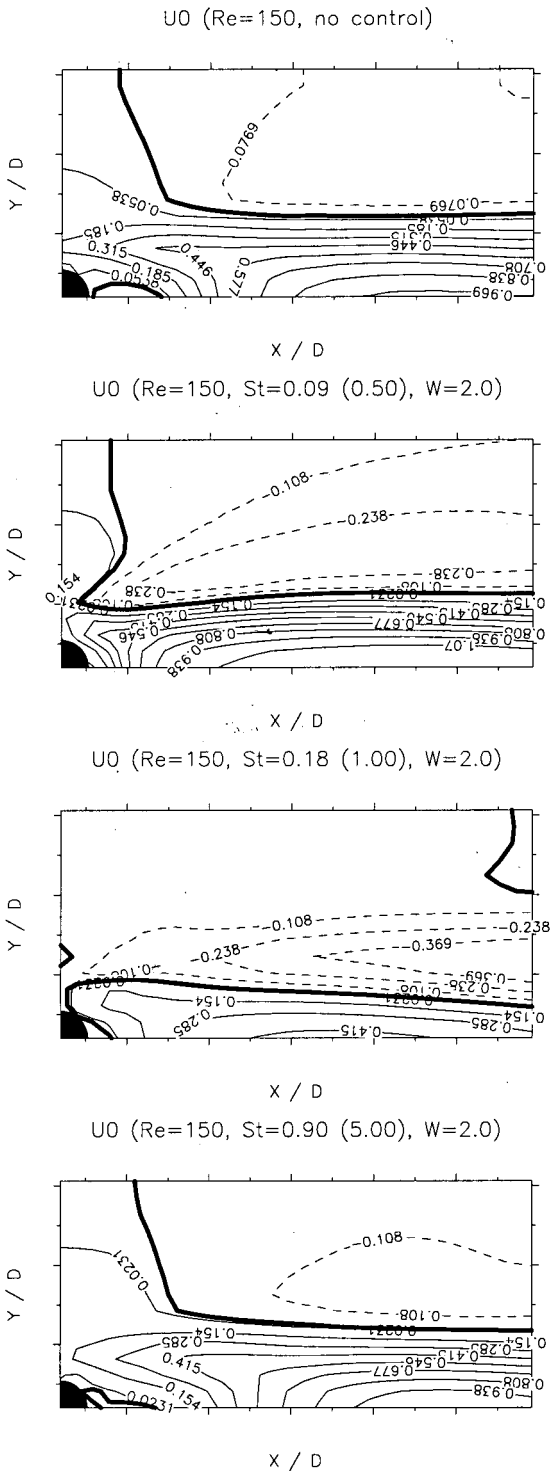

FIG. 13. Contour plots of the mean flow correction $u_0 = u_m - u_b$ for the flow without forcing and the cases A, C, and G. Numbers given in parentheses are the relative forcing frequencies $\mathrm{St}_f/\mathrm{St}_{\mathrm{nat}}$. The thick lines correspond to $u_m = 0$.

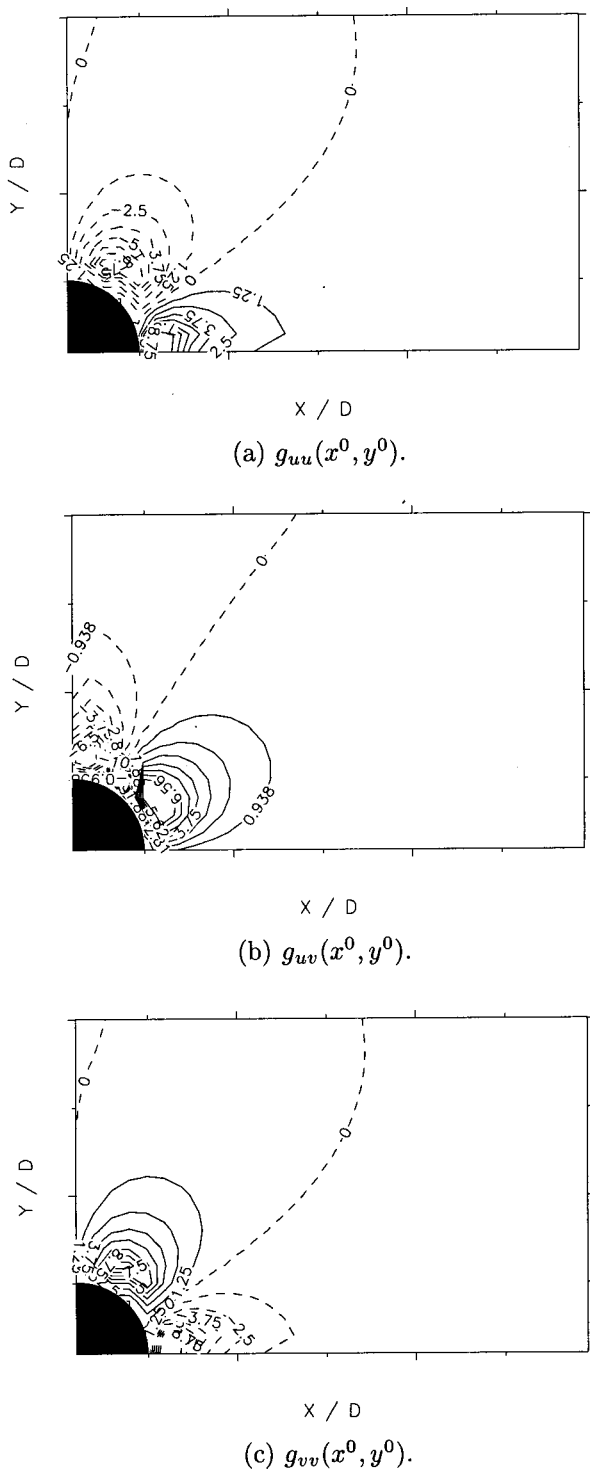

FIG. 14. Contour plots of the weights $g_{uu}(x^0,y^0) = \oint_{\Gamma_0} (\partial^2/\partial x \partial x)\, G(x,y,x^0,y^0)|_{\Gamma_0} n_x d\sigma$ (top), $g_{uv}(x^0,y^0) = 2\oint_{\Gamma_0} (\partial^2/\partial x \partial y) \times G(x,y,x^0,y^0)|_{\Gamma_0} n_x d\sigma$ (middle), and $g_{vv}(x^0,y^0) = \oint_{\Gamma_0} (\partial^2/\partial y \partial y) \times G(x,y,x^0,y^0)|_{\Gamma_0} n_x d\sigma$ (bottom). Owing to symmetry properties, in all the cases we show only the upper half of the flow domain.

centerline, so in Fig. 14 they are shown in the upper half of the flow domain only. We note that all of the quantities g_{uu}, g_{uv}, and g_{vv} have different signs in different parts of the flow domain, which means that, depending on the point where they are acting, the Reynolds stresses may either increase or decrease the pressure drag. This allows us to establish a link between the observed changes of drag and the modifications of the Reynolds stresses due to control. We remark here that these considerations are true when the mean velocity fields in the compared flows do not differ much (case G and the uncontrolled flow), since otherwise there may be additional modifications due to changes in the fields p^{0b} and p^{0bc}. In Figs. 15, 16, and 17 we show the distribu-

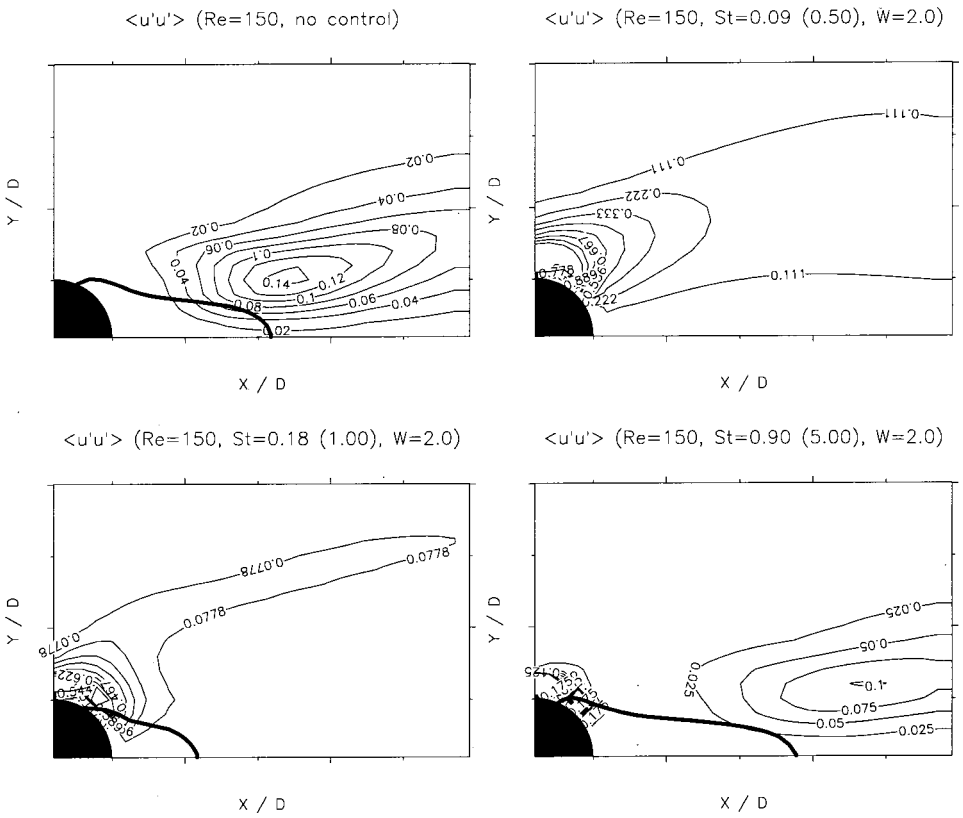

FIG. 15. Contour plots of the streamwise normal Reynolds stresses $\langle u'u' \rangle$ for the flow without forcing and the cases A, C, and G. Numbers given in parentheses are the relative forcing frequencies $\mathrm{St}_f/\mathrm{St}_{\mathrm{nat}}$. Thick lines mark the boundaries of the recirculation bubbles.

tions of the streamwise normal, shear, and cross-flow normal Reynolds stresses obtained in the simulations of the uncontrolled flow and the flows with the forcing conditions A, C, and G. In the figures, except for the ones corresponding to the case A, where it is virtually nonexistent, we indicate the boundary of the recirculation region. The streamwise and cross-flow normal stresses are symmetric, and the shear stresses antisymmetric, with respect to the centerline, hence

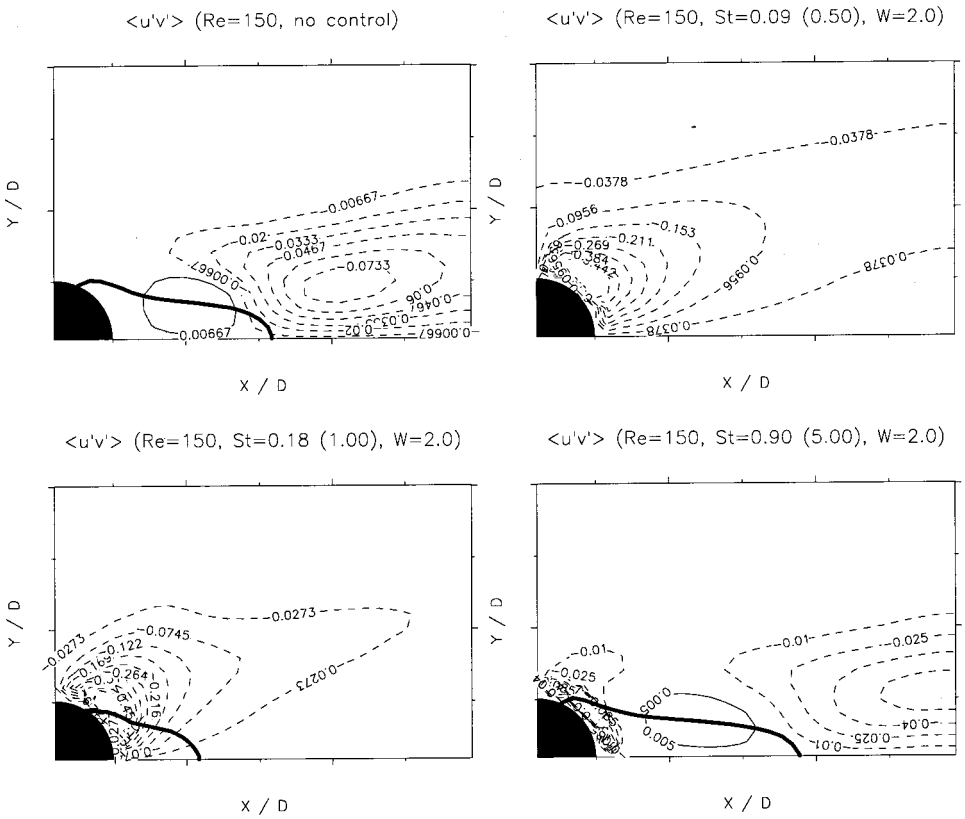

FIG. 16. Contour plots the shear Reynolds stresses $\langle u'v' \rangle$ for the flow without forcing and the cases A, C, and G. Numbers given in parentheses are the relative forcing frequencies $\mathrm{St}_f/\mathrm{St}_{\mathrm{nat}}$. Thick lines mark the boundaries of the recirculation bubbles.

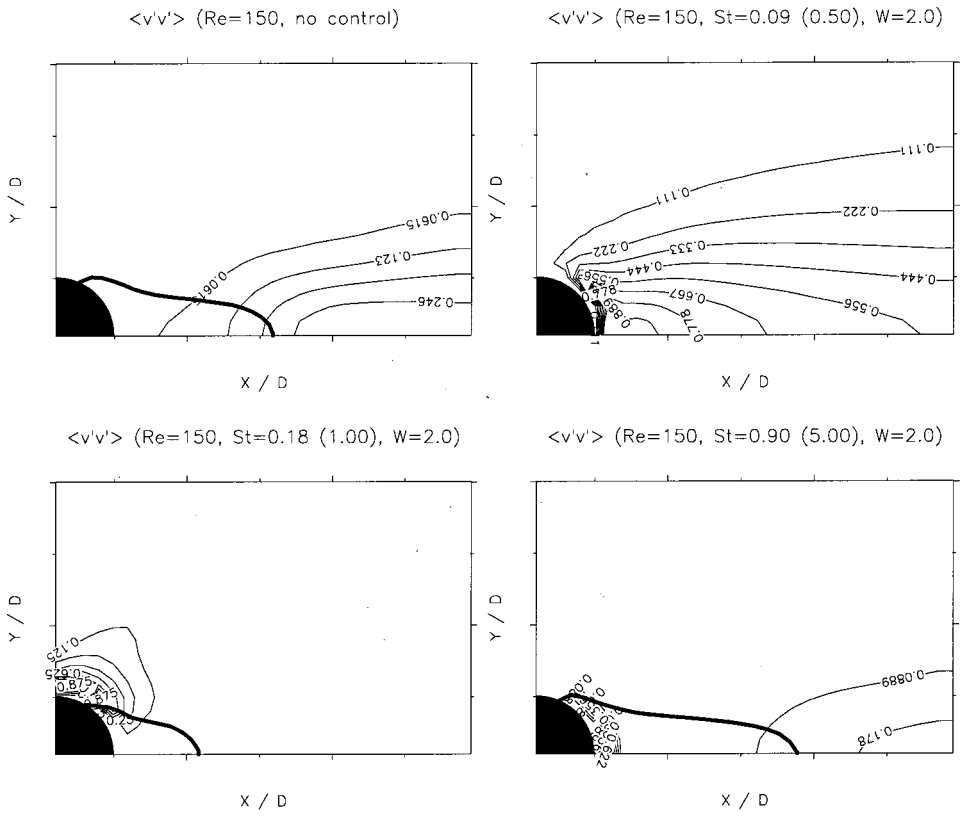

FIG. 17. Contour plots the cross-flow normal Reynolds stresses $\langle v'v' \rangle$ for the flow without forcing and the cases A, C, and G. Numbers given in parentheses are the relative forcing frequencies $\mathrm{St}_f/\mathrm{St}_{\mathrm{nat}}$. Thick lines mark the boundaries of the recirculation bubbles.

the results are presented for the upper part of the flow domain only. We note that as regards the uncontrolled flow our results are consistent with the data presented by Balachandar *et al.* in Ref. 34. The distribution of $\langle u'u' \rangle$ in the flow with no forcing is characterized by a maximum located away from the flow axis and slightly removed from the recirculation bubble. In the case G (high-frequency forcing) this distribution appears similar, but the maximum is weaker and removed farther downstream. There is also a region of nonzero stresses near the upper boundary of the cylinder. This difference can now be interpreted using the contour plots in Fig. 14(a), where we see that when the Reynolds stresses are acting farther downstream, their contribution to the pressure drag is smaller. Furthermore, as shown in Appendix A, the drag due to p^{0rs} is proportional to the magnitude of the Reynolds stresses and that is smaller in the case G. We also note that the region of nonzero stresses close to the upper boundary (case G) coincides with negative values of g_{uu} [Fig. 14(a)], so it has the effect of decreasing the pressure drag. The cases A and C (subharmonic and resonant forcing) are characterized by regions of strong streamwise normal stresses extending downstream away from the centerline. As regards the shear stresses $\langle u'v' \rangle$, in the cases A and C the maxima also extend downstream away from the centerline. In the uncontrolled flow and in the flow with the forcing conditions G there is a region of positive stresses just behind the obstacle followed by a region with negative stresses (note that below the centerline the senses of the stresses would be reversed). In the case G the magnitude of the shear stresses is lower than in the uncontrolled flow. Apart from this, just behind the cylinder there is a region of nonzero stresses. It corresponds to the entrainment of the fluid adjacent to the boundary by the rotating cylinder. Contour plots in Fig. 14(b) can be used to interpret these results. We note that the negative shear stresses acting close to the rear cylinder boundary in case G coincide with strongly positive values of g_{uv} in Fig. 14(b), and as a result yield a negative contribution to the pressure drag. As regards the cross-flow normal Reynolds stresses $\langle v'v' \rangle$, the distributions in the uncontrolled flow and in the case G are again similar, the main difference being that in the latter case the downstream region is noticeably weaker and there is a region with intense stresses just behind the obstacle. It corresponds to negative values of $g_{vv}(x^0,y^0)$ in Fig. 14(c) and therefore has the effect of decreasing the pressure drag. The cross-flow normal stresses $\langle v'v' \rangle$ in the subharmonic case A exist in a large region behind the obstacle and are confined to a relatively small area close to the upper boundary of the obstacle in the resonant case C. We noted before (cf. Figs. 8 and 9) that the mean flows corresponding to the two cases (the uncontrolled flow and the case G) were fairly similar and it can be therefore concluded that it is the modified distribution of the Reynolds stresses that is the major difference between these flows in terms of their mean characteristics. This difference also accounts for the drag decrease observed in the case G.

V. CONCLUSIONS

In this paper we have addressed various physical mechanisms that underlie modifications of drag in wake flows with rotary control. We examined the data obtained in the numerical simulations using the vortex method. In agreement with

the previous studies, we found that at higher forcing frequencies the drag is reduced. Interestingly, the obtained values were always slightly higher than the drag of the corresponding basic flow. The drag decrease observed at high forcing frequencies was lower than in other studies conducted at higher Re (e.g., Tokumaru and Dimotakis,[4] Lu and Sato,[6] Shiels and Leonard,[8] Cheng *et al.*,[14] and He *et al.*[15]). The reason for this is that at higher Re the drag of the basic flow is significantly lower [cf. Fig. 3(a)] and therefore the drag of the mean flow correction, i.e., the *controllable* contribution, is relatively bigger. This is why one can expect the control at higher Re to be more effective in terms of drag reduction. At the low Reynolds number studied here the control was found to be energetically inefficient, as the control power always exceeded the gain in the drag power.

The controlled flows were investigated here from the perspective of their mean velocity profiles and the associated fields of the Reynolds stresses. We have identified the following properties of the mean fields in the flows characterized by drag reduction (cases G and H), as compared to the uncontrolled flow.

(i) The mean flows in both cases are relatively similar, except for the elongation of the recirculation bubble in the controlled flow.
(ii) The magnitude of the Reynolds stresses in the downstream regions of the controlled flows is significantly decreased.
(iii) In the controlled flows regions of nonzero Reynolds stresses are present close to the rear and upper boundary of the cylinder and, as is evident from the Figs. 14(a)–14(c), they all have the effect of decreasing the drag.

Similarly, the following are the distinguishing features of the mean fields in the flows with the increased drag (cases A, B, C, and D).

(a) Very strong, positive mean flow correction in the near wake resulting in a significant shortening, or even suppression, of the recirculation bubble.
(b) Large magnitude of the Reynolds stresses acting away from the centerline.

The above changes of the mean velocity and Reynolds stress fields illustrate the mechanisms associated with modifications of drag. In accordance with the arguments presented in Sec. II, we conclude that it is the modified distribution and decreased magnitude of the Reynolds stresses in certain areas that are responsible for the observed drag reduction in some of the controlled flows. Comparing to the flows with increased drag, the modifications of the mean fields in the flows with reduced drag do not appear very profound, but also the drag decrease was rather moderate (approximately 25% compared to an over 100% drag increase in the ''worst'' case). It may be therefore concluded that the flows with high-frequency forcing do not reveal strong mean field effects and the drag reduction is mainly the result of the modifications of the Reynolds stresses. This finding is also consistent with observations of the flow patterns in controlled flows made by Cheng *et al.*[14] Obviously, changes of the Reynolds stress distribution reflect the modifications of the vortex shedding pattern, since the following two descriptions: in terms of the mean fields and the vortex dynamics, are equivalent. In particular, weakening of the Reynolds stresses acting downstream of the obstacle is related to the lower intensity of the vortex shedding observed in the flows with reduced drag. We also showed evidence that all the forced flows with reduced drag are characterized by an elongated recirculation bubble and, conversely, in the flows with increased drag the recirculation bubble is shrunk. This shows that the recirculation length L_{RB} serves as a ''footprint'' of the rotary control. Comparing our results with other studies, we concluded that under different conditions (different Re and oscillation amplitude W) the general trends are preserved, although the specific behavior of the controlled flows may be somewhat different. The above findings also imply that the Reynolds stresses are required to completely characterize the mean properties of a time-dependent flow.

ACKNOWLEDGMENTS

The first author acknowledges the financial support of the Polish State Committee for Scientific Research (Grant No. KBN 7 T07A 007 16), and the programs POLONIUM (Grant No. 99158) and GDR-CNRS ''Turbulence.'' Part of the computations were performed at ICM UW and PJWSTK. We have benefitted from the discussions with A. Styczek, J. Rokicki, and J. Szumbarski. Shankar Subramaniam kindly provided us with his optimized SIMPLEX solver.

APPENDIX A: INFLUENCE OF THE REYNOLDS STRESS DISTRIBUTION ON THE PRESSURE DRAG

We perform here qualitative analysis of the solutions to the system (8). Our goal is to see how changes in the Reynolds distribution and magnitude affect the quantity $\oint_{\Gamma_0} p^{0rs} n_x d\sigma$, i.e., the corresponding pressure drag. System (8) is a homogeneous Neumann problem for the Poisson equation in an unbounded exterior domain of a unit disk representing the obstacle. Its solution thus has the form

$$p^{0rs}(x,y) = -\int_{\Omega} G(x,y,x^0,y^0)\,\frac{\partial}{\partial x_k^0}\,\frac{\partial}{\partial x_j^0}\langle u_k' u_j'\rangle dx^0 dy^0, \tag{A1}$$

where $G(x,y,x^0,y^0)$ is the corresponding Green's function, which also accounts for the presence of the boundary. Here we use the obvious notation $x_1=x$, $x_2=y$, $u_1'=u'$, $u_2'=v'$, and a summation is implied when indices are repeated $(k,j=1,2)$. The quantities with the superscript ''0'' correspond to the location of the source point. Using the method of image points the Green's function can be constructed as (for conciseness we use here complex notation with $i=\sqrt{-1}$)

$$G(x,y,x^0,y^0) = -\frac{1}{2\pi}\left(\ln|(x-x^0)+i(y-y^0)| + \ln\left|x+iy-\frac{1}{x^0-iy^0}\right|\right). \tag{A2}$$

Now we integrate the expression (A1) by parts twice and obtain

$$p^{0rs}(x,y) = -\int_\Omega \frac{\partial^2}{\partial x_k^0 \partial x_j^0} G(x,y,x^0,y^0)\langle u_k' u_j'\rangle dx^0 dy^0 + \oint_{\Gamma_0}\left(\frac{\partial}{\partial x_j^0} G(x,y,x^0,y^0)\langle u_n' u_j'\rangle - G(x,y,x^0,y^0)\frac{\partial}{\partial x_j^0}\langle u_n' u_j'\rangle \right) d\sigma. \tag{A3}$$

For the case of the rotating cylinder the wall–normal velocity fluctuations u_n' are uniformly zero, so the integrand expression $(\partial/\partial x_j^0)\, G(x,y,x^0,y^0)\langle u_n' u_j'\rangle$ vanishes. As regards the second term in the boundary integral, we expand the derivative of the Reynolds stress,

$$\frac{\partial}{\partial x_j^0}\langle u_n' u_j'\rangle = \left\langle \frac{\partial u_n'}{\partial x_j^0} u_j' + u_n' \frac{\partial u_j'}{\partial x_j^0}\right\rangle = \left\langle \frac{\partial u_n'}{\partial x_j^0} u_j'\right\rangle, \tag{A4}$$

and then reexpress the derivatives in the polar coordinate system as

$$\frac{\partial u_n'}{\partial x_j^0} = \frac{\partial u_n'}{\partial r}\frac{\partial r}{\partial x_j^0} + \frac{\partial u_n'}{\partial \varphi}\frac{\partial \varphi}{\partial x_j^0}. \tag{A5}$$

Wall–normal velocity fluctuations do not vary with the azimuthal angle, so $\partial u_n'/\partial\varphi = 0$. By the continuity equation we obtain

$$\frac{\partial u_n'}{\partial r} = -\frac{u_n'}{r} - \frac{1}{r}\frac{\partial u_\varphi'}{\partial \varphi} = 0. \tag{A6}$$

Consequently, we have $\partial u_n'/\partial x_j^0 = 0$, $j = 1,2$, which by (A4) allows us to conclude that the second integrand in the boundary integral in (A3) also vanishes, and the pressure p^{0rs} is given by

$$p^{0rs}(x,y) = -\int_\Omega \frac{\partial^2}{\partial x^0 \partial x^0} G(x,y,x^0,y^0)\langle u'u'\rangle dx^0 dy^0 - 2\int_\Omega \frac{\partial^2}{\partial x^0 \partial y^0} G(x,y,x^0,y^0)\langle u'v'\rangle dx^0 dy^0 - \int_\Omega \frac{\partial^2}{\partial y^0 \partial y^0} G(x,y,x^0,y^0)\langle v'v'\rangle dx^0 dy^0. \tag{A7}$$

We note, first of all, that p^{0rs} is directly proportional to the magnitude of the Reynolds stresses. Furthermore, knowing the analytical expressions for $(\partial^2/\partial x^0 \partial x^0)\, G(x,y,x^0,y^0)$, $(\partial^2/\partial x^0 \partial y^0)\, G(x,y,x^0,y^0)$, and $(\partial^2/\partial y^0 \partial y^0)\, G(x,y,x^0,y^0)$ we can assess how the Reynolds stresses in the different parts of the flow domain contribute to p^{0rs} on the boundary, and consequently to the pressure drag $\oint_{\Gamma_0} p^{0rs} n_x d\sigma$. We thus have

$$\oint_{\Gamma_0} p^{0rs} n_x d\sigma = -\oint_{\Gamma_0}\left(\int_\Omega \frac{\partial^2}{\partial x^0 \partial x^0} G(x,y,x^0,y^0)\Big|_{\Gamma_0} \langle u'u'\rangle dx^0 dy^0\right) n_x d\sigma - 2\oint_{\Gamma_0}\left(\int_\Omega \frac{\partial^2}{\partial x^0 \partial y^0} G(x,y,x^0,y^0)\Big|_{\Gamma_0} \langle u'v'\rangle dx^0 dy^0\right) n_x d\sigma - \oint_{\Gamma_0}\left(\int_\Omega \frac{\partial^2}{\partial y^0 \partial y^0} G(x,y,x^0,y^0)\Big|_{\Gamma_0} \langle v'v'\rangle dx^0 dy^0\right) n_x d\sigma, \tag{A8}$$

which upon changing the order of integration and denoting

$$g_{uu}(x^0,y^0) = -\oint_{\Gamma_0} (\partial^2/\partial x^0 \partial x^0)\, G(x,y,x^0,y^0)|_{\Gamma_0} n_x d\sigma,$$

$$g_{uv}(x^0,y^0) = -2\oint_{\Gamma_0} (\partial^2/\partial x^0 \partial y^0)\, G(x,y,x^0,y^0)|_{\Gamma_0} n_x d\sigma$$

and

$$g_{vv}(x^0,y^0) = -\oint_{\Gamma_0} (\partial^2/\partial y^0 \partial y^0)\, G(x,y,x^0,y^0)|_{\Gamma_0} n_x d\sigma$$

[the subscript $|_{\Gamma_0}$ meaning evaluation with (x,y) on the boundary] gives

$$\oint_{\Gamma_0} p^{0rs} n_x d\sigma = \int_\Omega g_{uu}\langle u'u'\rangle d\Omega + \int_\Omega g_{uv}\langle u'v'\rangle d\Omega + \int_\Omega g_{vv}\langle v'v'\rangle d\Omega. \tag{A9}$$

In Figs. 14 we show the contour plots of g_{uu}, g_{uv}, and g_{vv} in the flow domain. The value at a given point (x^0,y^0) has the meaning of the geometric weight characterizing the relative contribution to pressure drag of the unit strength Reynolds stresses acting at this point.

APPENDIX B: VORTEX METHOD

The vortex method is a Lagrangian approach to solving the system (9)–(10). The motivation for choosing this particular solution method is that it is essentially grid-free, which allows one to easily handle various boundary conditions (including moving boundaries, etc.). The state of the art of the vortex methods is presented in the recent book by Cottet and Koumoutsakos[35] and references quoted therein. Here we make a few remarks on the design and implementation of the vortex method used in the present study.

Fundamental to all vortex methods is the approximation of the vorticity field using a superposition of vorticity particles,

$$\omega(\mathbf{x}) \cong \tilde{\omega}(\mathbf{x}) = \sum_{k=1}^{N} \Gamma_k \xi_\sigma(|\mathbf{x}-\mathbf{x}_k|), \tag{B1}$$

where $\mathbf{x}_k=[x_k,y_k]$ is the location of the kth particle, Γ_k is circulation and σ is the core radius. The function $\xi_\sigma(r)$ represents the axially symmetric distribution of vorticity within the support of the particle and in the present study is chosen as $\xi_\sigma(|\mathbf{x}|)=1/(2\pi\sigma^2)\, e^{-|\mathbf{x}|^2/(2\sigma^2)}$, which is motivated by simplicity and the second-order rate of convergence achieved by formula (B1). It is ensured that at all times the cores of the particles overlap. Every vorticity particle is displaced in the velocity field induced by all the remaining particles through the Biot–Savart law complemented with some additional potential velocity field accounting for the presence of solid boundaries,

$$\frac{d\mathbf{x}_k}{dt} = \sum_{\substack{j=1 \\ j\neq k}}^{N} \Gamma_j K_\sigma(\mathbf{x}_k,\mathbf{x}_j) + \nabla\Phi, \quad k=1,\ldots,N. \tag{B2}$$

Here K_σ represents a regularization of the Biot–Savart kernel $K(\mathbf{x},\mathbf{x}')=(1/2\pi)\{[-(y-y'),(x-x')]/|\mathbf{x}-\mathbf{x}'|^2\}$ computed as the following convolution:

$$K_\sigma(\mathbf{x}_k,\mathbf{x}_j) = \int_\Omega K(\mathbf{x}_k,\mathbf{x}')\,\xi_\sigma(\mathbf{x}'-\mathbf{x}_j)\,dx'. \tag{B3}$$

The number of particles N used in our simulations is quite large, usually on the order of $O(10^5-10^6)$, so in the evaluation of particle interaction we use the fast multipole method (FMM) developed by Greengard and Rokhlin in Ref. 36. An application of this algorithm reduces the computational cost from $O(N^2)$ operations to approximately $O(N\log N)$. In the present investigation we use the implementation of the algorithm described by Styczek and Wald in Ref. 37. Viscous diffusion is handled using the vorticity redistribution algorithm of Shankar and van Dommelen.[38] For every particle this approach uses a weak approximation of the diffusion kernel on an unstructured grid leading to an underdetermined algebraic system that is solved using a standard SIMPLEX technique. If the system of the neighboring vortices is too sparse or too irregular to ensure the existence of solutions to the SIMPLEX problem, new particles are added in the vicinity of the vortex whose diffusion is computed. Thus, this mechanism constantly maintains regularity of the Lagrangian approximation. This is necessary, since advection acts to distort the particle grid. In our simulations new vorticity is created in the form of a singular vortex sheet characterized by linear circulation density $\gamma(s)$. As shown by Prager in Ref. 39, the strength of the sheet is governed by the boundary integral equation of the form

$$\gamma(s) - \frac{1}{\pi} \oint_\Gamma \frac{\partial}{\partial n} \ln|\mathbf{x}(s)-\mathbf{x}(s')|\,\gamma(s')\,ds' = -2V_b^\tau, \tag{B4}$$

where s and s' are the arclength coordinates and V_b^τ is the boundary value of the tangential velocity component. In the case when the obstacle is a circular cylinder the solution of this system is available in analytical form. In the present study hydrodynamic forces are computed using the variational approach developed by Protas *et al.* in Ref. 40. This method allows for the efficient calculation of forces using only velocity and vorticity fields. As mentioned in Sec. II, in our investigation some attention will be given to the basic flow, i.e., the unstable steady symmetric solution of the Navier–Stokes system at a supercritical value of Re. Using the vortex method such a solution is obtained by ensuring at every time step that the systems of vortices above and below the centerline are mirror reflections of each other. This inhibits the growth of any symmetry-breaking perturbations and ensures that the flow remains symmetric.

[1] B. J. A. Zielińska and J.-E. Wesfreid, "On the spatial structure of global modes in wake flow," Phys. Fluids **7**, 1418 (1995).
[2] B. J. A. Zielińska, S. Goujon-Durand, J. Dušek, and J.-E. Wesfreid, "Strongly nonlinear effect in unstable wakes," Phys. Rev. Lett. **79**, 3893 (1997).
[3] S. Taneda, "Visual observations of the flow past a circular cylinder performing rotary oscillation," J. Phys. Soc. Jpn. **45**, 1038 (1978).
[4] P. Tokumaru and P. Dimotakis, "Rotary oscillation control of a cylinder wake," J. Fluid Mech. **224**, 71 (1991).
[5] J. R. Filler, P. L. Marston, and W. C. Mih, "Response of the shear layers separating from the circular cylinder to small-amplitude rotational oscillations," J. Fluid Mech. **231**, 481 (1991).
[6] X.-Y. Lu and J. Sato, "A numerical study of flow past a rotationally oscillating circular cylinder," J. Fluids Struct. **10**, 829 (1996).
[7] D. Shiels, Ph.D. thesis, California Institute of Technology, 1998.
[8] D. Shiels and A. Leonard, "Investigation of drag reduction on a circular cylinder in rotary oscillation," J. Fluid Mech. **431**, 297 (2001).
[9] S.-J. Baek and H. J. Sung, "Numerical simulation of the flow behind a rotary oscillating circular cylinder," Phys. Fluids **10**, 869 (1998).
[10] S.-J. Baek and H. J. Sung, "Quasi-periodicity in the wake of a rotationally oscillating cylinder," J. Fluid Mech. **408**, 275 (2000).
[11] N. Fujisawa, K. Ikemoto, and K. Nagaja, "Vortex shedding resonance from a rotationally oscillating cylinder," Fluids Struct. **12**, 1041 (1998).
[12] N. Fujisawa and Y. Kawaji, "Active control of vortex shedding from a circular cylinder by rotary oscillations," Proceedings of the 10th Symposium on Turbulent Shear Flows, University Park, PA (1995), pp. 14, 25.
[13] S.-J. Baek, S. B. Lee, and H. J. Sung, "Response of a circular cylinder wake to superharmonic oscillation," J. Fluid Mech. **442**, 67 (2001).
[14] M. Cheng, Y. T. Chew, and S. C. Luo, "Numerical investigation of a rotationally oscillating cylinder in a mean flow," Fluids Struct. **15**, 981 (2001).
[15] J. W. He, R. Glowinski, R. Metcalfe, A. Nordlander, and J. Periaux, "Active control and drag optimization for flow past circular cylinder," J. Comput. Phys. **163**, 83 (2000).
[16] C. Mathis, M. Provansal, and L. Boyer, "The Bénard–von Kármán instability: transient and forced regimes," J. Fluid Mech. **182**, 1 (1987).
[17] J. Dušek, P. Le Gal, and Ph. Fraunie, "A numerical and theoretical study of the first Hopf bifurcation in a cylinder wake," J. Fluid Mech. **264**, 59 (1994).
[18] J. Dušek, "Spatial structure of the Bénard–von Kármán instability," Eur. J. Mech. B/Fluids **15**, 619 (1996).
[19] J.-E. Wesfreid, S. Goujon-Durand, and B. Zielińska, "Global mode behavior of the streamwise velocity in wakes," J. Phys. II **6**, 1343 (1996).
[20] A. D. D. Craik, *Wave Interactions and Fluid Flows* (Cambridge University Press, Cambridge, 1985).
[21] A. Maurel, V. Pagneux, and J.-E. Wesfreid, "Mean flow correction as a non-linear saturation mechanism," Europhys. Lett. **32**, 217 (1995).
[22] R. D. Henderson, "Details of the drag curve near the onset of vortex shedding," Phys. Fluids **7**, 2102 (1995).
[23] R. Mittal and S. Balachandar, "Effects of three-dimensionality on lift and drag of nominally two-dimensional cylinders," Phys. Fluids **7**, 1841 (1995).
[24] M. D. Gunzburger and J. S. Peterson, "Finite-element methods for the streamfunction-vorticity equations: Boundary-condition treatments and multiply connected domains," SIAM (Soc. Ind. Appl. Math.) J. Sci. Stat. Comput. **9**, 650 (1988).

[25]A. Nowakowski, J. Rokicki, and A. Styczek, ''The pressure problem in the stochastic vortex blob method,'' *Vortex Flows and Related Numerical Methods*, ESAIM 101-110, edited by H. Cottet, Y. Gagnon, A. Giovannini, and E. Meiburg, http://www.emath.fr/proc/Vol.1/, 1996.
[26]B. Protas, Ph.D. thesis, Warsaw University of Technology and Université Pierre et Marie Curie, 2000.
[27]C. Wieselberger, ''Neurere feststellungen über die gesetze des flussigkeits- und luftwiederstands,'' Phys. Z. **22**, 321 (1921).
[28]B. Fornberg, ''Steady viscous flow past a circular cylinder up to Reynolds number 600,'' J. Comput. Phys. **61**, 297 (1985).
[29]R. D. Henderson (private communication).
[30]U. Fey, M. König, and H. Eckelmann, ''A new Strouhal–Reynolds-number relationship for the circular cylinder in the range $47<\mathrm{Re}<2\times10^5$,'' Phys. Fluids **10**, 1547 (1998).
[31]M. Coutanceau and R. Bouard, ''Experimental determination of the main features of the viscous flow in the wake of a circular cylinder in uniform translation. Part 1. Steady flow,'' J. Fluid Mech. **79**, 231 (1977).
[32]S. Goujon-Durand, J.-E. Wesfreid, and P. Jenffer, ''Contrôle actif du sillage autour d'un cylindre oscillant,'' Proceedings of the 15th French Congress of Mechanics, Nancy, 2001 (available at http://www.cfm2001.ciril.fr), p. 659.
[33]J. C. S. Lai and M. F. Platzer, ''The jet characteristics of a plunging airfoil,'' 36th Aerospace Sciences Meeting and Exhibit, Reno, NV, 1998, AIAA Pap. 98-0101.
[34]S. Balachandar, R. Mittal, and F. M. Najjar, ''Properties of the mean recirculation region of two-dimensional bluff bodies,'' J. Fluid Mech. **351**, 167 (1997).
[35]G.-H. Cottet and P. Koumoutsakos, *Vortex Methods: Theory and Practice* (Cambridge University Press, Cambridge, 2000).
[36]L. Greengard and V. Rokhlin, ''A fast algorithm for particle simulations,'' J. Comput. Phys. **73**, 325 (1987).
[37]A. Styczek and P. Wald, ''Fast and efficient vortex blob simulation of the flow past the circular cylinder,'' Arch. Mech. **52**, 281 (1995).
[38]S. Shankar and L. van Dommelen, ''A new diffusion procedure for vortex methods,'' J. Comput. Phys. **127**, 88 (1996).
[39]W. Prager, ''Die druckverteilung an körpern in ebener potentialströmung,'' Phys. Z. **29**, 865 (1928).
[40]B. Protas, A. Styczek, and A. Nowakowski, ''An effective approach to computation of forces in viscous incompressible flows,'' J. Comput. Phys. **159**, 231 (2000).